ROBUST TURBULENCE LOAD ALLEVIATION

Natascha Jansson[1] **and David Eller**[1]

[1]Department of Aeronautical and Vehicle Engineering
Royal Institute of Technology
SE 100 44 Stockholm, Sweden
natascha@kth.se

Keywords: robust control theory, aeroservoelasticity, flight simulation.

Abstract: Using a comparatively detailed aeroelastic model for a generic commuter aircraft, a turbulence load alleviation system is designed with the objective of reducing structural fatigue. An $\mathcal{H}_\infty$-optimal controller for the nominal model is found to be highly sensitive to small disturbances in the control system dynamics, so that a slightly perturbed closed-loop model is destabilized. Robust control methods are exploited to construct an alternative controller which improves robustness to disturbances at a small cost in nominal performance. Finally, fatigue loads experienced by the (open-loop and controlled) model are evaluated by means of two different load reconstruction methods, showing that the simpler modal displacement approach may introduce significant errors in wing bending moments.

1 INTRODUCTION

The presence of atmospheric turbulence is a very serious concern for a transport aircraft manufacturer. A distinction can be made between sudden strong *gusts* which may cause structural failure even after a single exposure, and more frequent but not as violent *turbulence* which can cause fatigue due to the large number of cycles. For this work a generic commuter aircraft has been the test object for the design of a controller with the objective to alleviate loads in turbulence.

Moulin and Karpel [1] have performed gust load alleviation for a transport aircraft and performed wind tunnel experiments to determine the efficiency of the control law. Gust load alleviation using *feedback* (as opposed to *feedforward*) control has been managed, an appreciable achievement with respect to the sudden development of a wind gust. For this work feedback control is again implemented to provide load alleviation and the implementation of methods based on robust control theory allow a systematic consideration of modeling errors. The mathematical methods used for the state-space description of the aircraft is similar to the methods used here. The estimation of the structural loads in the state-space description used for both this work and by Moulin and Karpel only utilizes the less accurate modal displacement method (MD). However, in this work the modal acceleration method (MA) is implemented in a post-processing step to improve the accuracy of the structural load approximations.

Even though it has been shown that is possible to use feedback control even for gust load alleviation, the fast dynamics of a wind gust favor the use of feedforward control. The development of forward-looking lidar sensors, presented by Rabadan, Schmitt, Pistner and Rehm [2], leads the way for such possibilities to use feed-forward control for alleviation

of gust load. The improvements this technique can offer with the possibility to predict gusts are of course very interesting, but not considered for the present work.

2 THEORY AND MODELING

2.1 Equations of motion

To describe the motion of the aircraft a combination of the motion of the center of gravity and the elastic deformation of the airframe is utilized. The motion of the center of gravity is limited to vertical translation, z, and rotation about the lateral axis, θ, in the body-fixed coordinate system. The velocity, U_0, along the longitudinal axis is assumed to be constant, allowing the motion in that direction to be excluded from the analysis, except for its contribution to the dynamic pressure. The orientation of the body-fixed coordinate system is illustrated in Figure 1.

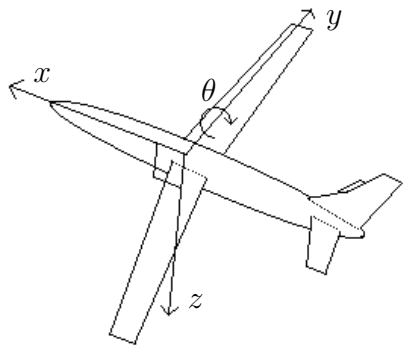

Figure 1: Body-fixed coordinate system used to describe the rigid-body motion.

For the simulation model the elastic deformation is described by a linear combination of a limited set of modes of free vibration. These modes form a basis which is chosen as the six symmetric modes of lowest order. The free vibration modes will be included in the set of states by six coefficients, $\eta_1, ..., \eta_6$, representing the amplitude of each elastic mode. It is assumed that these low-order modes can describe the dynamics of the deformation in a sufficiently accurate manner.

Load alleviation is attempted using symmetric deflection of elevators, δ_e, flaps, δ_f, and ailerons, δ_a. The angular acceleration is controlled by applying a torque at each control surface hinge. These moments at the control surfaces are used as the control variables in the control law design as

$$\boldsymbol{u}_c = [M_e \quad M_a \quad M_f]^T, \tag{1}$$

where the subscripts represent the elevators, the ailerons and the flaps of the aircraft respectively.

The complete motion of the aircraft can be divided into rigid body motion

$$\boldsymbol{\xi}_{r.b.} = [z \ \theta]^T, \tag{2}$$

the elastic deformation of the structure

$$\boldsymbol{\xi}_{e.d.} = [\eta_1 ... \ \eta_6]^T, \tag{3}$$

and the control surface deflections

$$\boldsymbol{\xi}_{c.s.} = [\delta_e \ \delta_a \ \delta_f]^T. \tag{4}$$

The time derivatives of all variables are also included in the complete set of states. Finally there has been a choice of three additional aerodynamic state for each of the flight mechanical states, elastic modal states and control surface deflections, according to

$$\boldsymbol{\xi}_{a.} = [\xi_{a,1} ... \ \xi_{a,33}]^T, \tag{5}$$

as explained in Section 2.2.

The complete vector of states is then

$$\boldsymbol{\xi} = \begin{bmatrix} \boldsymbol{\xi}_{r.b.} \\ \boldsymbol{\xi}_{e.d.} \\ \boldsymbol{\xi}_{c.s.} \\ \dot{\boldsymbol{\xi}}_{r.b.} \\ \dot{\boldsymbol{\xi}}_{e.d.} \\ \dot{\boldsymbol{\xi}}_{c.s.} \\ \boldsymbol{\xi}_{a} \end{bmatrix}. \tag{6}$$

The mass and elastic properties of the aircraft are given by a beam model implemented in Nastran [3]. For a general aerodynamic transfer function matrix $\boldsymbol{Q}(s)$ the equations of motion is defined in the Laplace domain using the Laplace variable s according to

$$s^2\boldsymbol{M}\begin{bmatrix} \boldsymbol{\xi}_{r.b.}(s) \\ \boldsymbol{\xi}_{e.d.}(s) \\ \boldsymbol{\xi}_{c.s.}(s) \end{bmatrix} + s\boldsymbol{C}\begin{bmatrix} \boldsymbol{\xi}_{r.b.}(s) \\ \boldsymbol{\xi}_{e.d.}(s) \\ \boldsymbol{\xi}_{c.s.}(s) \end{bmatrix} + \boldsymbol{K}\begin{bmatrix} \boldsymbol{\xi}_{r.b.}(s) \\ \boldsymbol{\xi}_{e.d.}(s) \\ \boldsymbol{\xi}_{c.s.}(s) \end{bmatrix} = q_\infty \boldsymbol{Q}(s)\begin{bmatrix} \boldsymbol{\xi}_{r.b.}(s) \\ \boldsymbol{\xi}_{e.d.}(s) \\ \boldsymbol{\xi}_{c.s.}(s) \end{bmatrix}. \tag{7}$$

In Equation (7) the diagonal mass matrix $\boldsymbol{M}$ is given by

$$\boldsymbol{M} = \begin{bmatrix} m & & & & & & \\ & I_{yy} & & & & & \\ & & I_{elev.} & & & & \\ & & & I_{ail.} & & & \\ & & & & I_{flap} & & \\ & & & & & \boldsymbol{I} \end{bmatrix}, \tag{8}$$

the diagonal stiffness matrix $\boldsymbol{K}$ in Equation (7) is given by

$$\boldsymbol{K} = \begin{bmatrix} 0 & & & & & & \\ & 0 & & & & & \\ & & k_{elev.} & & & & \\ & & & k_{ail.} & & & \\ & & & & k_{flap} & & \\ & & & & & \boldsymbol{\Omega^2} \end{bmatrix}, \tag{9}$$

and due to the choice of coordinate system for the motion of the center of gravity the damping matrix $\boldsymbol{C}$ has one off-diagonal element according to

$$\boldsymbol{C} = \begin{bmatrix} \begin{bmatrix} 0 & -mU_0 \\ 0 & 0 \end{bmatrix} & & \\ & 0 & \\ & & \ddots \end{bmatrix}, \tag{10}$$

where m is the mass of the aircraft, I_{yy} is the mass moment of inertia around the lateral axis of the aircraft, $I_{elev.}$, $I_{ail.}$ and I_{flap} are the mass moment of inertia of the different control surfaces around their respective hinge lines, the unit matrix is the generalized mass matrix corresponding to the modal coordinates, $k_{elev.}$, $k_{ail.}$ and k_{flap} are hinge stiffnesses for the different control surfaces and $\boldsymbol{\Omega^2}$ is the generalized stiffness matrix corresponding to the modal coordinates.

As indicated by the diagonal properties of the mass matrix and stiffness matrix in Equation (8) and (9) the inertial and elastic coupling of control surface deflection and other states has been neglected.

2.2 Aerodynamic model

Aerodynamic data is obtained for a simplified wetted-surface mesh of the aircraft using a potential flow solver [4]. The aerodynamic response for a change in angle of attack, deformation in any of the elastic modes, as well as for displacement of each control surface is evaluated for a set of reduced frequencies.

Unsteady aerodynamic effects are included by fitting data for the range of reduced frequencies to rational aerodynamic functions according to the theory described in [5], giving rise to a number of additional aerodynamic states, ξ_a. By assuming that it is possible to approximate each aerodynamic term separately it is possible to use Roger's approximation [6]. The original set of aerodynamic transfer function matrices for undamped motion $\boldsymbol{Q}(ik)$ is replaced with the rational aerodynamic approximation $\tilde{\boldsymbol{Q}}(ik)$ according to

$$\boldsymbol{Q}(ik) \approx \tilde{\boldsymbol{Q}}(ik) = \boldsymbol{A}_0 + \boldsymbol{A}_1(ik) + \boldsymbol{A}_2(ik)^2 + \ + \boldsymbol{D}(\boldsymbol{I}(ik) - \boldsymbol{R})^{-1}\boldsymbol{E}(ik), \tag{11}$$

where $\boldsymbol{D}$, $\boldsymbol{R}$ and $\boldsymbol{E}$ are given by

$$\boldsymbol{D} = [\boldsymbol{I}\ \boldsymbol{I} \cdots], \boldsymbol{R} = -\begin{bmatrix} \gamma_1\boldsymbol{I} & & \\ & \gamma_2\boldsymbol{I} & \\ & & \ddots \end{bmatrix}, \boldsymbol{E} = \begin{bmatrix} \boldsymbol{A}_3 \\ \boldsymbol{A}_4 \\ \vdots \end{bmatrix}, \tag{12}$$

and the matrices $\boldsymbol{A}_0, \boldsymbol{A}_1, ...$ contains real valued coefficients that give rise to the $\tilde{\boldsymbol{Q}}(ik)$ resulting in the best match to $\boldsymbol{Q}(ik)$ in a least squares sense. The constants $\gamma_1, \gamma_2, ...$ in Equation (12) must be selected before the rational aerodynamic approximation fitting is performed, but the method for this choice is unfortunately not detailed by Roger [6].

To suit the state-space description the rational aerodynamic approximation $\tilde{\boldsymbol{Q}}(ik)$ is first transformed to be a function of the Laplace variable s as

$$\tilde{\boldsymbol{Q}}(s) = \boldsymbol{A}_0 + \frac{L}{U_0}\boldsymbol{A}_1 s + \frac{L^2}{U_0^2}\boldsymbol{A}_2 s^2 + \boldsymbol{D}(\boldsymbol{I}s - \frac{U_0}{L}\boldsymbol{R})^{-1}\boldsymbol{E}\ s, \tag{13}$$

then a vector of augmented aerodynamic states is defined as

$$\boldsymbol{\xi}_a(s) = (\boldsymbol{I}s - \frac{U_0}{L}\boldsymbol{R})^{-1}\boldsymbol{E}\ s \begin{bmatrix} \boldsymbol{\xi}_{r.b.}(s) \\ \boldsymbol{\xi}_{e.d.}(s) \\ \boldsymbol{\xi}_{c.s.}(s) \end{bmatrix}. \tag{14}$$

2.3 State-space model

For the control law design, a state space representation of the aircraft is used, requiring a set of output variables to be regulated. For this implementation the output variables are the vertical position of the center of gravity, the pitch angle and the wing root bending moment contribution from the six retained elastic modes, M_B. The reduced measure of the wing root bending moment is calculated as a linear combination of the eigenmode amplitudes, $\eta_1, ..., \eta_6$. The vector of output variables is

$$\boldsymbol{\psi} = [z \quad \theta \quad M_B]^T. \tag{15}$$

The state-space representation is given by

$$\dot{\boldsymbol{\xi}} = \boldsymbol{A}\boldsymbol{\xi} + \boldsymbol{B}\boldsymbol{u}_c + \boldsymbol{B}_{\tilde{\boldsymbol{d}}}\tilde{d} \tag{16}$$

$$\boldsymbol{\psi} = \boldsymbol{C}\boldsymbol{\xi} + \boldsymbol{D}\boldsymbol{u}_c \tag{17}$$

as a linear system of equations where all of the states represent differences from an initial set of states, $\boldsymbol{\xi}_0$, as does the control variables represent differences from the original set of control variables, $\boldsymbol{u}_{c,0}$ and finally the output variables represent deviations from the initial values of those output variables, $\boldsymbol{\psi}_0$. The disturbance $\tilde{d}$ is the vertical velocity of the atmospheric turbulence.

Equation (16) describes the total equations of motion for the aircraft, and the matrices in that equation contain inertial, elastic and aerodynamic properties according to

$$\boldsymbol{A} = \begin{bmatrix} 0 & \boldsymbol{I} & 0 \\ \tilde{\boldsymbol{M}}^{-1}[q_\infty \boldsymbol{A}_0 - \boldsymbol{K}] & \tilde{\boldsymbol{M}}^{-1}[\frac{q_\infty L}{U_0}\boldsymbol{A}_1 - \boldsymbol{C}] & \tilde{\boldsymbol{M}}^{-1}[q_\infty \boldsymbol{D}] \\ 0 & \boldsymbol{E} & \frac{U_0}{L}\boldsymbol{R} \end{bmatrix}, \tag{18}$$

$$\boldsymbol{B} = \begin{bmatrix} 0 \\ \tilde{\boldsymbol{M}}^{-1}[\boldsymbol{I}] \\ 0 \end{bmatrix} \tag{19}$$

and

$$\boldsymbol{B}_{\tilde{\boldsymbol{d}}} = \begin{bmatrix} 0 \\ \tilde{\boldsymbol{M}}^{-1}[-\frac{q_\infty}{U_0}\boldsymbol{A}_{0,\theta}] \\ 0 \end{bmatrix}, \tag{20}$$

where $\tilde{\boldsymbol{M}}$ is defined according to

$$\tilde{\boldsymbol{M}} = \boldsymbol{M} - \frac{q_\infty L^2}{U_0^2}\boldsymbol{A}_2, \tag{21}$$

and $\boldsymbol{A}_{0,\theta}$ is the column in $\boldsymbol{A}_0$ corresponding to the aerodynamic forces due to a displacement in θ.

2.4 Atmospheric turbulence model

Turbulence is included in the model as a disturbance, d, which is assumed to be Gaussian white noise of unit intensity and zero mean. It is then passed through a linear filter, W_d, generating a gust disturbance, $\tilde{d}$, with the Dryden power spectral density [7]. The transfer function of W_d is given by

$$W_d = \sqrt{\frac{3U_0\sigma_w^2}{\pi L_w}}\frac{\frac{U_0}{\sqrt{3}L_w} + s}{[\frac{U_0}{L_w} + s]^2}, \tag{22}$$

where σ_w is the RMS of the vertical gust velocity and L_w is the scale of turbulence, set to a fixed value [7].

The disturbance is then included into the state-space model as a change in angle of attack, related to the aircraft trim velocity as

$$\alpha_{\tilde{d}} = \arctan\frac{-\tilde{d}}{U_0}. \tag{23}$$

Since the aircraft trim velocity is significantly larger than the gust velocity (23) can be linearized according to

$$\alpha_{\tilde{d}} \approx \frac{-\tilde{d}}{U_0}. \tag{24}$$

It should be noted that the aerodynamic effect of this change in angle of attack, $\alpha_{\tilde{d}}$, is treated as if it was a change in the pitch angle, θ, but without any effect on the inertia forces.

2.5 Robust control problem

No matter how much effort is being put into the production of a precise numerical model, no model describes a physical system flawlessly. The need for using methods of robust control theory is based on this fact and a desire to handle uncertainties in a structured manner. With traditional control theory one aims to find an optimal controller for the nominal system, while robust control theory is implemented in methods used to assure stability and performance for any system similar to the nominal system but with some quantified uncertainty.

Such uncertainties can be modeled in many ways, with more or less physical insight. Here an output multiplicative perturbation model is chosen. This perturbation model allows all three outputs to vary without detailed knowledge of which physical errors could cause these perturbations. The closed loop system is shown in Figure 2.

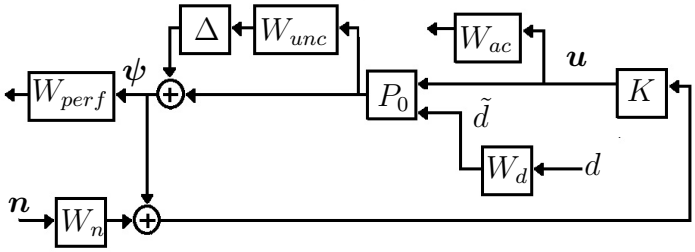

Figure 2: Robust control problem.

The included blocks represent the nominal plant P_0 defined by Equations (16) and(17), the controller, K, the performance weight for the output signals, W_{perf}, the actuator weight, W_{ac}, the linear Dryden power spectral density filter, W_d, the weight on the noise in the system, W_n, and the weighting functions representing the uncertainties in the system at the output of the nominal system, W_{unc}. The uncertainties are modeled as multiplicative uncertainties and are given as products of the uncertainty weight functions and the perturbations Δ. The complex-valued perturbations Δ can have any phase, but must satisfy

$$||\Delta|| \leq 1. \tag{25}$$

As a starting point for the robust control design a controller is designed for the nominal system, i.e. the system without any modeling uncertainties. This controller is produced using $\mathcal{H}_\infty$ synthesis [8] and for the design of an $\mathcal{H}_\infty$ controller the plant shown in Figure 2 is redrawn as illustrated in Figure 3. In that figure the upper loop, with the variables $\boldsymbol{z_\Delta}$ and $\boldsymbol{v_\Delta}$, represent the uncertainties and therefore that part is ignored for the design of the $\mathcal{H}_\infty$ controller. The uncertainty input variables $\boldsymbol{z_\Delta}$ should not be confused with the state variable z, which represents the vertical position of the aircraft. The input variable $\boldsymbol{w}$ contains both the atmospheric disturbance d and the noise $\boldsymbol{n}$. The output variable $\boldsymbol{e}$ represents the tracking error. The MATLAB function `hinfsyn` from the Robust Control Toolbox is used for the $\mathcal{H}_\infty$ synthesis.

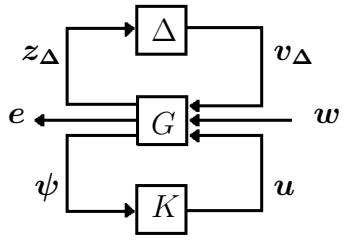

Figure 3: System description used for the design of the nominal $\mathcal{H}_\infty$ controller.

The initial $\mathcal{H}_\infty$ controller is used as a basis for the design of a robust controller. To develop the robust controller the system is redrawn again, to suit the μ-synthesis. For

the μ-synthesis [8] it is useful to have the system described as a LFT (Linear Fractional Transformation), as shown in Figure 4.

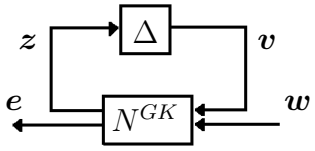

Figure 4: System used for the μ-synthesis design of the robust controller.

In Figure 4, $N^{GK}(s)$ represents the closed-loop plant as a lower LFT, $F_l()$, according to $N^{GK}(s) = F_l(G(s), K(s))$, using the notations from Figure 3. This system representation is used to define the conditions for nominal performance as

$$||N^{GK}_{2,2}(s)||_\infty < 1, \tag{26}$$

the condition for robust stability as

$$||N^{GK}_{1,1}(s)||_\infty < 1 \tag{27}$$

and the condition for robust performance, using the notation $F_u()$ for the upper LFT, according to

$$||F_u(N^{GK}(s), \Delta(s))||_\infty < 1 \tag{28}$$

where $N^{GK}_{i,j}$ is the part of N^{GK} describing the transfer function from input j to output i according to Figure 5.

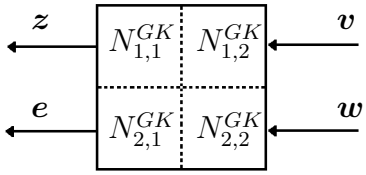

Figure 5: Division of plant N^{GK} into transfer functions from the two inputs to the two outputs.

Nominal performance, robust stability and robust performance of the system is evaluated using the MATLAB function `mussv` from the Robust Control Toolbox. To design a robust controller a method called D-K iteration is intended to be used to achieve robust performance. However, in this case the demand for robust performance can be achieved already with the initial $\mathcal{H}_\infty$ synthesis by choosing the weight functions in a proper way, and therefore this controller is chosen as the robust controller.

In addition to the robust controller another controller is designed using $\mathcal{H}_\infty$ synthesis for the nominal system, this controller will for this work be referred to as the $\mathcal{H}_\infty$ controller.

The weight functions for the design of the $\mathcal{H}_\infty$ controller are not chosen to suit the design of a robust controller, but to strive after optimal control of the nominal system.

2.6 Test case

The structural finite-element model is based on a single configuration case of the Saab 340 turboprop commuter aircraft. Modal analysis results are modified to approximately include control surface effects as described above. Frequency-domain aerodynamic response data is computed by means of a wetted surface mesh based on a simplified geometry model of the Saab 340B. Due to the modifications applied, the resulting aeroelastic model is not representative of the Saab 340 aircraft. The Nastran model consists mainly of beam elements and has about 9800 degrees of freedom, while the aerodynamic mesh features 65 000 triangular surface elements.

3 LOAD ANALYSIS

In order to recover structural loads from the simulated system, a frequency domain approach is chosen. The driving factor in this decision is the fact that a description of unsteady aerodynamic loads is available in the form of complex-valued pressure distributions caused by harmonic excitation of deformations modeshapes. In the present case, these modeshapes are free vibration modes of the structure, but the aerodynamic analysis is not restricted to that particular choice. The construction of a state-space model similar to Equation (11) for the full set of surface pressure coefficients (about 32 000 values) was determined to be an unattractive option because of the very substantial computational effort required.

3.1 Frequency domain aerodynamic load basis

An excitation of the modeshape z_j with frequency ω results in structural displacements $u(t) = z_j e^{i\omega t}$. In order to determine the aerodynamic response to this unsteady deformation, it must be expressed in terms of aerodynamic mesh coordinates. In the present case, the structural model consists mainly of beam elements while the aerodynamic configuration is represented by a wetted surface mesh, so that an accurate mapping of aerodynamic to structural mesh motion is not straightforward. Therefore, a nodal mapping procedure based on radial basis functions (RBF) is employed, where the motion of an aerodynamic mesh vertex is expressed in terms of basis functions $\phi(r)$ according to

$$\boldsymbol{u}_a = \sum_k \boldsymbol{w}_k \phi(r_k), \quad \text{where} \quad r_k = \sqrt{|\boldsymbol{x}_a - \boldsymbol{x}_k|^2}. \tag{29}$$

Here, $\boldsymbol{w}_k$ is the 3-component vector weight associated with the center $\boldsymbol{x}_k$ and $\boldsymbol{x}_a$ is the point where the interpolation is to be evaluated. In order to determine the weights, the location of the centers $\boldsymbol{x}_k$ must be fixed. For the present case, a set of geometrically unique structural nodes is chosen as centers. Weights are then computed by solving the dense linear system resulting from the requirement that the interpolation (29) matches a known structural displacement field. In general, this will be a overdetermined system which is solved with multiple right-hand sides – one for each modeshape – resulting in one

set of RBF weights for each mode. Aerodynamic mesh deformations are then obtained by evaluating (29) for each mesh vertex. Frequency-domain aerodynamic loads are computed by means of a boundary element method for linear potential flow, where harmonically varying mesh deformation is accounted for by transpiration wall boundary conditions. The resulting solution is one complex-valued vector of surface pressure coefficients $\hat{\boldsymbol{c}}_p^j(\omega)$ associated with the excitation of deformation shape j with angular frequency ω. Pressures are then integrated over each aerodynamic element to yield a single force acting on the element center. Aerodynamic element forces are then transformed into a force and moment pair acting on the geometrically nearest structural node. The loading of the structural model caused by rigid-body motion and structural displacements can hence be expressed as

$$\boldsymbol{f}_a(\omega) = q_\infty \sum_j \boldsymbol{Q}_j(\omega)\Xi_j(\omega), \tag{30}$$

where $\Xi_j(\omega)$ is the frequency domain coordinate of deformation mode j – that is, the Fourier transform of $\xi_j(t)$ – q_∞ is the dynamic pressure and $\boldsymbol{Q}_j(\omega)$ the mapping of $\hat{\boldsymbol{c}}_p^j(\omega)$ to the structural model. Note that the load basis $\boldsymbol{Q}_j(\omega)$ is not, in general, a simple function of the angular frequency. Instead, it is usually only known at a number of discrete values of the reduced frequency.

3.2 Turbulence load evaluation

According to Hoblit [7], the result a continuous gust load analysis is commonly expressed as an graph of frequency of exceedance, that is, as the number of times $N(y_L)$ that a given load level y_L is reached per flight time. Here, the load y_L can be any relevant variable. For the commuter aircraft test case, the vertical plane wing bending moment just outboard of the fuselage-wing junction is selected. As the strength of atmospheric turbulence varies significantly with altitude, a proper gust load analysis requires knowledge or assumptions about the mission profile of the aircraft of interest. Only flight at sea level is considered in the analysis presented here, which results in considerably higher gust loads than a more realistic flight profile would. The frequency of exceedance is computed as

$$N(y_L) = N_0 \left(P_1 \exp\left(-\frac{y_L}{\bar{A} b_1} \right) + P_2 \exp\left(-\frac{y_L}{\bar{A} b_2} \right) \right), \tag{31}$$

where P_1, P_2, b_1 and b_2 are altitude-dependent constants characterizing the probability distribution of gust velocity magnitudes. In the examples to follow, these constants are taken from [7] for flight at sea level, as listed in Table 1. $\bar{A}$ and N_0 in Equation (31) are

$b_1 = 3.7$	$b_2 = 7.7$
$P_1 = 0.005$	$P_2 = 1.0$

Table 1: Gust probability coefficients for sea level flight.

determined by integration of the power spectral density (PSD) of the output y_L according

to

$$\bar{A} = \sqrt{\int_0^\infty |H(f)|^2 \Phi_g(f) df} \tag{32}$$

$$N_0 = \frac{1}{\bar{A}} \sqrt{\int_0^\infty f^2 |H(f)|^2 \Phi_g(f) df}. \tag{33}$$

In the above, $\Phi_g(f)$ is the power spectral density of the gust velocity (22) for unit σ_w and $H(f)$ the frequency-response function (FRF) relating the gust velocity to the load output variable y_L. In general, $H(f)$ is derived from the equations of motion of the aircraft using varying levels of simplification.

3.3 Modal displacement FRF

Using the modal displacement approximation, displacements (and, proportionally, element forces) are assumed to be well represented by the modal basis selected for the analysis. In that case, the force output is obtained by means of multiplication of the state variables with a constant vector $\boldsymbol{c}_{y\xi}$ as in

$$y_L(f) = \boldsymbol{c}_{y\xi}^T \Xi(f) = \boldsymbol{c}_{y\xi}^T G_w(f) d'(f), \quad \text{so that} \quad H_M(f) = \boldsymbol{c}_{y\xi}^T G_w(f), \tag{34}$$

where the transfer function $G_w(f)$, obtained from the state-space system (16) for the open loop system and from the plant shown in Figure 2 for the closed loop system, relates a frequency-domain gust velocity input to the state variables $\Xi(f)$.

3.4 Modal acceleration FRF

When the approximations introduced by the modal displacement (MD) method are unacceptable, an alternative approach is the modal acceleration (MA) method. In this case, it is assumed that velocities and accelerations are well captured by the modal subspace, while deformations are not. Hence, accelerations $\ddot{\boldsymbol{u}}(t)$ are expressed in terms of modal coordinates using $\ddot{\boldsymbol{u}}(t) = \boldsymbol{Z}\ddot{\boldsymbol{\xi}}(t)$. In the frequency domain, the discrete equation of motion becomes

$$-\omega^2 \boldsymbol{M}\boldsymbol{Z}\Xi(\omega) + \boldsymbol{K}\boldsymbol{U}(\omega) = \boldsymbol{f}_a(\omega). \tag{35}$$

Inserting the relation $\Xi(f) = G_w(f)d'(f)$ into Equation (30), frequency-domain aerodynamic forces $f_a(f)$ are computed according to

$$\boldsymbol{f}_a(f) = q_\infty \boldsymbol{Q}_\xi(f) G_w(f) d'(f) + \boldsymbol{f}_w(f). \tag{36}$$

Here, the additional force vector $\boldsymbol{f}_w(f)$ represents the aerodynamic forces caused by the gust. In general, the gust forces can be written as

$$\boldsymbol{f}_w(f) = q_\infty \boldsymbol{q}_w(f) d'(f). \tag{37}$$

The modal acceleration frequency response function $H_R(f)$ is then defined by

$$H_R(f) = \boldsymbol{c}_{yu}^T q_\infty \boldsymbol{K}^{-1} \left[((2\pi f)^2 \boldsymbol{M} P_e + \boldsymbol{Q}(f)) G_w(f) + \boldsymbol{q}_w(f) \right] \tag{38}$$

where $\boldsymbol{c}_{yu}$ is a constant vector which relates deformations to the desired force or strain output according to $y_L(f) = \boldsymbol{c}_{yu}^T \boldsymbol{U}(f)$. For an unconstrained aircraft, $\boldsymbol{K}$ is singular, and Equation (38) is solved using the inertial relief option available in Nastran. This option generates additional loads caused by the rigid-body acceleration resulting from the applied loading. Therefore, rigid-body acceleration contributions are not included in the load vector created for the evaluation of H_R, which is indicated by the inclusion of the projection P_e in Equation (38).

4 RESULTS AND DISCUSSION

4.1 Effect of load evaluation procedure

Figures 6 and 7 show a comparison of the frequency response functions obtained using the modal displacement (MD) and modal acceleration methods, named $H_M(f)$ (MD, Equation 34) and $H_R(f)$ (MA, Equation 38) above, for two different output quantities y_L. The graphs marked with a cross symbol are obtained using the open-loop system, while the graphs marked with a circle are for the closed-loop system including the nominal $\mathcal{H}_\infty$ controller. For the frequency response function $H_R(f)$ the structural loads are calculated using the MA method, but it should be noted that the feed-back controller is still fed with the same output variables as for $H_M(f)$. For the open-loop case, H_M H_R are found to be

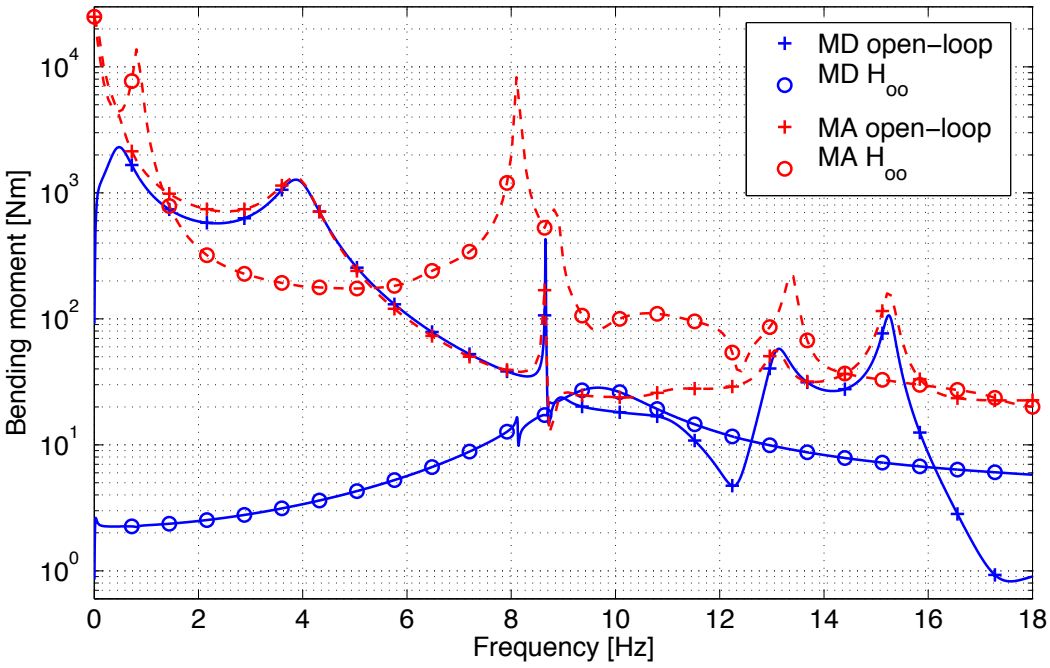

Figure 6: Absolute frequency response for wing root bending moment

fairly similar over a band of frequencies between 0.5 Hz and 9 Hz. Below and above these limits, the presumably more accurate MA response is substantially larger. For the low frequency region, this may be related to the fact that the selected modal subspace containing 6 free vibration modes may not be a particularly good basis for the representation

of static deformation [9]. Above 9 Hz, the actual deformation likely contains significant contributions of higher-frequency modes not included in the selected subspace. The large amplitude of the MA response at higher frequencies, and its comparatively slow rate of decrease with frequency contributes considerably to much larger continuous gust loads. In Figure 6, the wing root bending moment at the wing-fuselage junction is displayed. This is the target variable selected to be reduced by the $\mathcal{H}_\infty$ controller. As expected, the bending moment response of the closed-loop system is predicted to be reduced dramatically over the open-loop response, when evaluated using the simpler MD approach. Application of the MA method, however, shows significantly different pattern. Now, a reduction of the root bending moment can only be achieved for frequencies below 5.5 Hz.

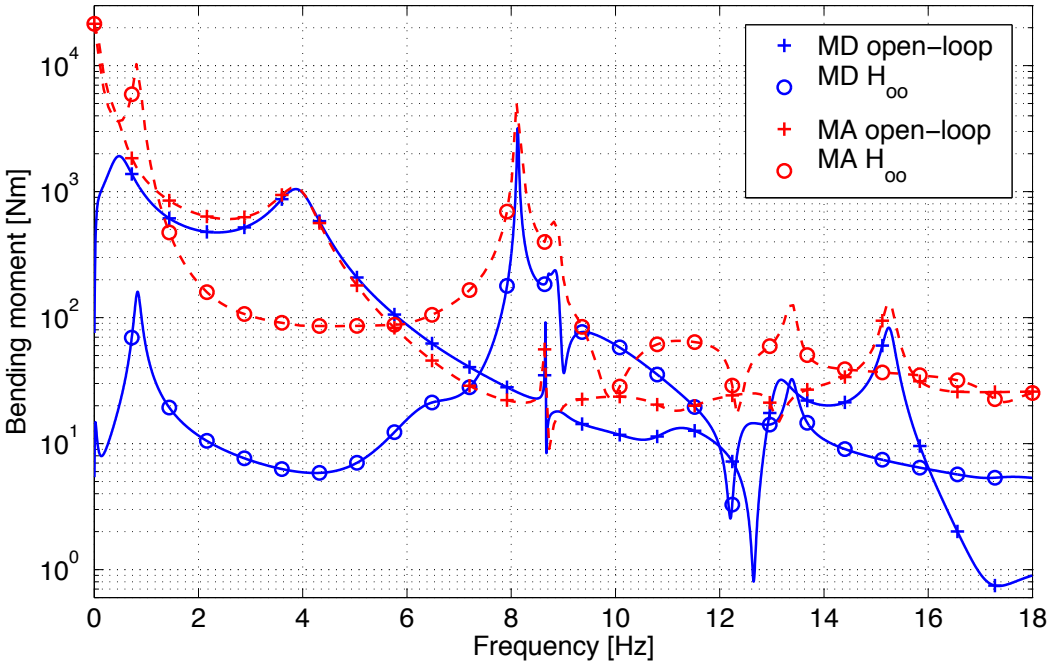

Figure 7: Absolute frequency response for inboard spar bending moment.

The response of the main wing spar bending moment about 2 m outboard of the wing-fuselage junction is shown in Figure 7. This output is not included in the controller synthesis, and as a consequence, not even the MD results show a similarly dramatic reduction as for the wing root bending moment. Again, the response reduction turns out to be less impressive still when evaluated using the MA approach. From the pattern observed in Figures 6 and 7, it appears that the synthesis of an $\mathcal{H}_\infty$ optimal controller is sensitive to the load evaluation method used. In fact, the substantial difference between MD and MA response of the closed-loop system shown in Figure 6 indicates that the controller synthesis 'exploits' the weakness of the MD load evaluation to achieve a low $\mathcal{H}_\infty$ cost value.

4.2 Exceeded load levels

The frequency response data computed by means of the modal acceleration method is used to compute the frequency of exceedance $N(y_L)$ according to Equation (31) for flight at sea level. In Table 2, root bending moment results are shown for a set of combinations of aeroelastic models and controllers. The column labeled *max* contains the load exceeded once per 5000 flight hours, the value labeled *LCF*, for low-cycle fatigue, is predicted to occur once per flight hour and the last column labeled *HCF*, high-cycle fatigue, is exceeded 500 times per hour. Results are given for both the nominal system and a perturbed configuration where all control surface hinge stiffnesses have been reduced by 3%. Note that that the $\mathcal{H}_\infty$-optimal controller destabilizes the perturbed system and is not listed. Exceeded load levels obtained using the modal acceleration method are substantially

	MD [kNm]			MA [kNm]		
	max	LCF	HCF	max	LCF	HCF
Nominal, open-loop	300.9	154.8	48.3	1100.0	525.3	106.1
Nominal, $\mathcal{H}_\infty$	6.9	3.8	1.6	1320.1	681.5	215.6
Nominal, robust	18.7	10.3	4.3	994.6	465.2	79.0
Perturbed, open-loop	300.6	154.7	48.3	1099.5	525.1	106.0
Perturbed, robust	22.9	12.6	5.2	997.2	467.7	81.4

Table 2: Turbulence load alleviation effects.

larger than those which result from application of the modal displacement approach, which is explained by the significantly larger magnitude of the response function shown in Figures 6 and 7. The nominal controller even generates higher loads than computed for the open-loop case, when evaluated with the MA method, which the robust controller does not.

5 CONCLUSIONS

The resulting structural loads obtained using the MD method are successfully reduced using control laws. An optimally designed $\mathcal{H}_\infty$ controller can substantially reduce fatigue loads caused by continuous turbulence, at least the loads considered for the control law design. For the test case considered, the magnitude of the reduction is so large that a considerably increased fatigue life would be possible. However, such a controller is sensitive to model inaccuracies, which, in some cases, may even lead to destabilization of the aeroservolelastic system. A robust controller design for which requirements on the structural singular value, μ, is considered can alleviate this sensitivity at the cost of reduced controller performance.

Employment of the MA method does, however, drastically change the results both considering the magnitude of the structural loads and the effectiveness of the control laws. It is concluded that the system description used for the design of the the controllers is not good enough. As seen in Figure 6 the wing root bending moment for the open-loop case using the MD method does not correspond closely to that of the MA method. It would be of interest to find a better agreement between these two responses, and one way could be

to use a frequency dependent linear combination of the elastic modes. This approach does however not directly translate to the time domain state-space representation required by the currently applied $\mathcal{H}_\infty$-synthesis tool `hinfsyn`.

6 ACKNOWLEDGEMENTS

The authors would like to thank Lars Helmersson, Torsten Bråmå and Bengt Mexnell of Saab Aerosystems AB who kindly provided data for the Saab 340 aircraft which was very helpful in the definition of the test case. This work was partially financed by the fifth Swedish National Aeronautics Research Program (NFFP-5).

7 REFERENCES

[1] B. Moulin and M. Karpel. Gust load alleviation using special control surfaces. *Journal of Aircraft*, 44(1):17–25, Jan.-Feb. 2007.

[2] T. Pistner G. J. Rabadan, N. P. Schmitt and W Rehm. Airborne lidar for automatic feedforward control of turbulent in-flight phenomena. *Journal of Aircraft*, 47(2):392–403, Mar.-Apr. 2010.

[3] *MSC.Nastran Version 70.5 Quick Reference Guide*, 1998.

[4] D. Eller and M. Carlsson. An efficient aerodynamic boundary element method and its experimental validation. *Aerospace Science and Technology*, 7(7):532–539, Nov. 2003.

[5] *ZAERO Version 6.4 Theoretical Manual*, 2003.

[6] K. L. Roger. Airplane math modeling methods for active control design. *AGARD-CP-228*, pages 4.1–4.11, 1977.

[7] F. M. Hoblit. *Gust Loads on Aircraft: Concepts and Applications*. AIAA, Inc., 1988.

[8] S. Skogestad and I. Postlewaite. *Multivariable Feedback Control: Analysis and Design*. John Wiley & Sons, 1996.

[9] R. L. Bisplinghoff, H. Ashley, and R. L. Halfman. *Aeroelasticity*. Dover Publications, 1955.